

# AllSpark : A Multimodal Spatio-Temporal General Intelligence Model with Thirteen Modalities

Run Shao, Cheng Yang, QiuJun Li, LinRui Xu, Xiang Yang, Xian Li, MengYao Li, Qing Zhu, Yongjun Zhang, YanSheng Li, Yu Liu, Yong Tang, Dapeng Liu, Shizhong Yang, Haifeng Li *Member, IEEE*,

**Abstract**—RGB, infrared, multispectral, and other spatio-temporal modal data fundamentally represent different observational approaches for the same geographic object. Therefore, leveraging multimodal data is an inherent requirement for comprehending geographic objects. However, due to the high heterogeneity in structure and semantics among various spatio-temporal modal data, the joint interpretation of multimodal spatio-temporal data has long been an extremely challenging problem. The primary challenge resides in striking a trade-off between the cohesion and autonomy of diverse modalities. This trade-off becomes progressively nonlinear as the number of modalities expands. Inspired by the human cognitive system and linguistic philosophy, where perceptual signals from the five senses converge into language, we introduce the Language as Reference Framework (LaRF), a fundamental principle for constructing a multimodal unified model. Building upon this, we propose a multimodal spatio-temporal general artificial intelligence model called AllSpark. Our model integrates thirteen different modalities into a unified framework, including one-dimensional (text, code), two-dimensional (RGB, infrared, SAR, multispectral, hyperspectral, tables, graphs, trajectory, oblique photography), and three-dimensional (point clouds, videos) modalities. To achieve modal cohesion, AllSpark uniformly maps diverse modal features to the language modality by a modal bridge and a multimodal large language models. To maintain modality autonomy, AllSpark introduces modality-specific encoders to extract the tokens of various spatio-temporal modalities. Finally, observing a gap between the model’s interpretability and downstream tasks, we designed modality-specific prompts and task heads to enhance the model’s generalization capability on specific downstream tasks. Experiments indicate that AllSpark, without expert knowledge of most spatio-temporal modalities and utilizing a unified structure, achieves competitive accuracy in modalities such as RGB and trajectory compared to state-of-the-art models. Moreover, AllSpark shows excellent adaptability in various modalities, such as MSI, HSI, PointCloud, table, code, and graph. AllSpark demonstrates the potential and possibility of constructing general artificial intelligence with a large language model. LaRF and AllSpark contribute to the shift in the research paradigm in spatio-temporal intelligence, transitioning



Fig. 1. We propose “Language as Reference Framework (LaRF)” as the fundamental principle for constructing multimodal models. Under the guidance of this principle, we introduced a multimodal general intelligence model, AllSpark, which integrates thirteen spatio-temporal modalities.

from a modality-specific and task-specific paradigm to a general paradigm.

**Index Terms**—Spatio-temporal Data, Multimodal Machine Learning, Large Language Model, General Intelligence Model.

## I. INTRODUCTION

**B**ENEFITING from the increasingly diverse observational methods available for spatio-temporal scenes, geographic objects can be described using various spatio-temporal modalities, such as RGB, infrared, SAR, multispectral, graph, and spatio-temporal trajectory data. Each modality provides unique information about different aspects of the geographic object. Analogous to the human process of perceiving and understanding the world through multiple modalities, such as vision, hearing, and touch, joint interpretation of multimodal data is an inherent requirement for intelligent models to achieve cognition of geographic objects.

However, due to the inherent differences in the mechanisms of each modality, various modalities are often highly heterogeneous in both structure and semantics. For example, in terms of structure, a table is composed of rows and columns. Point clouds are represented by three-dimensional coordinates along with various feature values. A text is composed of sequences of words. In terms of semantics, RGB imagery

The work was supported in part by the Major Program Project of Xiangjiang Laboratory under Grant 22XJ01010, in part by the National Natural Science Foundation of China under Grant 61973047 and Grant 42171458, and in part by using Computing Resources at the High-Performance Computing Platform of Central South University. (Corresponding author: Haifeng Li.)

Run Shao, Cheng Yang, QiuJun Li, LinRui Xu, Xiang Yang, Xian Li, MengYao Li and Haifeng Li are with the School of Geosciences and Info-Physics, Central South University, Changsha 410083, China, and also with the Xiangjiang Laboratory, Changsha 410205, China.

Qing Zhu is with the Faculty of Geosciences and Environmental Engineering, Southwest Jiaotong University, Chengdu 611756, China.

Yongjun Zhang and YanSheng Li are with School of Remote Sensing and Information Engineering, Wuhan University, Wuhan 430079, China.

Yu Liu is with the School of Earth and Space Sciences, Peking University, Beijing 100871, China.

Yong Tang, Dapeng Liu are Huawei Technologies Co., Ltd, China.

Shizhong Yang is with BDS Micro Chip Inc, Changsha 410071, China.

reflects the electromagnetic characteristics of visible light bands emitted and reflected by geographic objects, whereas SAR imagery reflects the electromagnetic characteristics of microwaves emitted actively by radar for scattering from geographic objects.

For a long time, constrained by the high heterogeneity across various modalities mentioned above, researchers have often developed specific methods based on prior assumptions related to a particular modality or designed multimodal approaches based on a few low-heterogeneity modalities. For instance, in single-modal research, C. R. Qi et al. proposed PointNet [1] for the point cloud modality, emphasizing the invariance of point cloud data ordering and the significance of global and local features. For language modality, Vaswani et al. introduced the transformer [2], which focuses on the long-range dependencies within word sequences. For the graph modality, Kipf and Welling proposed the GCN [3] based on the adjacency relationships between nodes in a graph. In multimodal research, the fusion of optical and SAR imagery has been widely explored in both traditional and deep learning remote sensing [4]. Moreover, visual-language models have undergone rapid development in recent years [5]–[9]. The diverse prior assumptions associated with each modality have resulted in significant gaps between methods designed for different modalities, making it challenging to perceive and understand different modalities using a unified model.

We believe that the key challenge in addressing this issue lies in striking a trade-off between the cohesion and autonomy of diverse modalities. Cohesion refers to the presence of mutually correlated shared information among modalities, while autonomy signifies the existence of unique information specific to each modality relative to others. If we simply project data from multiple modalities into a common representation space for fusion, emphasizing the cohesion between modalities, this approach may lead to the loss of modality-specific information, thereby diluting the essence of multimodal collaboration. In contrast, if we excessively stress the autonomy between modalities, it may hinder the establishment of connections among them, limiting the model’s ability to simultaneously perceive multiple modalities. Moreover, as the number of modalities increases, balancing cohesion and autonomy becomes progressively more challenging nonlinearly.

We observe that in the process of comprehending the world, humans integrate information from multiple modalities, such as hearing, touch, smell, and vision. The concepts formed through the parsing of these modalities ultimately converge in language. Humans engage in associating, reasoning, and expressive behaviours through language. In other words, language precisely encodes human perception and understanding of the world, providing clear definitions and meanings to abstract concepts from each modality. Inspired by this, we propose the **Language as Reference Framework (LaRF)** as a fundamental principle for constructing multimodal models. As illustrated in Figure 1, the abstract concepts derived from each modality should align with language, allowing for joint interpretation in the unified representation space of language.

Building upon this, we propose a multimodal spatio-temporal general artificial intelligence model, AllSpark,

that integrates thirteen different modalities into a unified framework, including one-dimensional (text, code), two-dimensional (RGB, infrared, SAR, multispectral, hyperspectral, tables, graphs, trajectory, oblique photography), and three-dimensional (point clouds, videos) modalities.

To achieve modal cohesion, AllSpark uniformly maps diverse modal features to the language modality. In addition, we designed modality-specific prompts to guide multimodal large language models in accurately perceiving multimodal data.

To maintain the autonomy between modalities, AllSpark introduces specific modal encoders for each modality to extract independent tokens. Given the high heterogeneity among modality data and modality encoders, a significant dimensional gap exists between the tokens of each modality and the language modality. To address this issue, we introduce a modality bridge, a mechanism from Lynx [10], to accomplish dimensional mapping from each modality’s tokens to the language tokens.

Finally, considering the existing gap between the interpretability of the multimodal large language model and the specific downstream tasks, we design task heads for each downstream task to enhance the model’s generalization capability. Given the powerful interpretability capabilities of the multimodal large language model, we adhere to a lightweight design principle in both the modal encoders and task heads.

Experiments demonstrate that AllSpark achieves competitive accuracy without expert knowledge in most modalities and utilizing a unified structure in modalities such as RGB and spatio-temporal trajectories compared to state-of-the-art models. Specifically, in the RGB modality, the accuracy of AllSpark is only 0.84 lower than that of the SOTA model, and in the trajectory modality, the average displacement error (ADE) metric differs by only 0.07 compared to that of the SOTA model. Additionally, AllSpark exhibits excellent adaptability in various other modalities, including point clouds, multispectral, hyperspectral, tables, graphs, and code. Theoretically, our proposed model has the potential for seamless extension to an arbitrary number of modalities.

In other words, our contributions can be summarized as follows:

- We first propose a unified multimodal spatio-temporal general model, AllSpark, that successfully integrates thirteen spatio-temporal modalities into a single model.
- Inspired by the human cognitive system and linguistic philosophy, we propose the language as reference framework (LaRF), which offers a novel solution to balance cohesion and autonomy among multiple modalities. This principle provides a fresh approach to multimodal unification.
- We propose new approaches for designing multimodal models in the spatio-temporal domain. AllSpark demonstrates the potential and ability to construct a general model with large language models, thereby contributing to the shift in the research paradigm in spatio-temporal intelligence, transitioning from a modality-specific and task-specific paradigm to a general paradigm.
- Experiments indicate that AllSpark, without expert knowledge of the majority of spatio-temporal modalities

and utilizing a unified structure, achieves competitive accuracy in modalities such as RGB and trajectory information compared to state-of-the-art models. Moreover, AllSpark shows excellent adaptability in various modalities, such as MSI, HSI, PointCloud, table, code, and graph. Theoretically, our proposed model has the potential for seamless extension to an arbitrary number of modalities.

## II. RELATED WORK

Leveraging multimodal data is an inherent requirement for achieving cognitive recognition of geospatial objects. An ideal multimodal model should possess the capability to integrate all the modalities for joint interpretation. Hence, a crucial trend in the research of intelligent methods in the spatio-temporal domain is the continual increase in the number of modalities available for joint interpretation. Initially, early researchers often constructed single-modal expert models based on prior assumptions about a specific modality, achieving remarkable success within each respective modality. In recent years, with a deeper understanding of single-modal interpretation methods, numerous researchers have attempted to integrate several low-heterogeneity modalities to construct multimodal interpretation approaches. However, as the number of modalities increases, the challenge of balancing cohesion and autonomy among the modalities becomes increasingly difficult. In the following, we recall the development of intelligent methods in the spatio-temporal domain from the perspective of the continually increasing number of modalities, and finally, we present the principles and approach of our proposed model, AllSpark.

### A. Single-Modal Model

For one-dimensional modalities, we focus on code and text. Code and text are both fundamental language modalities, but due to the excellent characteristics of code, such as strict syntax, unambiguous nature, and ability to interact with machines, code is treated as separate modality. Z. Feng et al. pretrained a model, CodeBERT [11], which facilitates the mutual transfer of information between code and natural language modalities. For the text modality, landmark contributions include a transformer [2], BERT [12], and the GPT series [13]–[16], which have inspired subsequent series of works.

We categorize RGB, multispectral, hyperspectral, infrared, SAR, table, graph, trajectory, and oblique photography as two-dimensional (2D) modalities.

Among the two-dimensional modalities, standard three-channel RGB images are among the most common. For the RGB modality, the ResNet [17] proposed by K. He et al., which is based on the importance of visual global and local information, and the visual transformer (ViT) [18] introduced by A. Dosovitskiy et al., which leverages a global attention mechanism, represent two landmark contributions.

An increase in the number of channels in images leads to multispectral and hyperspectral modalities. B. Huang et al. proposed the STDCNN [19], leveraging the characteristic of

a greater number of bands in multispectral images to simultaneously model the global spatial and spectral properties of multispectral images. In comparison to multispectral images, hyperspectral images have even more bands, often reaching hundreds. Based on this, X. Yang et al. introduced the R-3D-CNN [20] to further enhance the extraction of spectral features.

Beyond an increase in the number of bands, attention has been given to images captured in specific spectral bands. For instance, infrared images, widely applied in fields such as agriculture and oceanography, have gained significant attention. H. Chen et al. proposed a shallow convolutional neural network that integrates a decision tree to meet the demand for real-time intelligent interpretation of a large volume of infrared images in agricultural water resource monitoring [21]. In the case of SAR images formed by active microwave radar, S. Chen et al. introduced AConvNet [22], a widely used fully convolutional neural network for intelligent SAR image interpretation.

For oblique photography, 3D reconstruction aims to utilize single or multiple two-dimensional images from various viewpoints to reconstruct a three-dimensional model. Y. Yao et al. addressed this task by proposing MVSNet [23]. By utilizing techniques such as three-dimensional convolution, the model establishes correlations between images from different perspectives, thereby reconstructing a three-dimensional model of the target from the features extracted from two-dimensional images.

Beyond the visual domain, the table is one of the commonly used modalities for recording and expressing information. TabNet [24], proposed by S. Ö. Arik et al., employs a sequence attention mechanism to achieve feature selection in the Table modality, thereby enabling interpretable and more efficient learning.

The trajectory modality reflects the temporal changes in the spatial positions of objects. A. Gupta et al. proposed the social generative adversarial networks (GAN) [25] based on the characteristic of trajectory multiplicity. This model combines historical trajectory information with social context information to predict multiple plausible future outcomes.

For the graph modality, Kipf and Welling introduced the classic graph convolutional network (GCN) [3], which is based on the adjacency relationships between nodes in the graph. P. Veličković et al. proposed the GAT [26], which incorporates attention mechanisms into the graph modality.

Finally, we turn our attention to three-dimensional modalities: video and point clouds.

The video modality is formed by stacking images over time. A model proposed by A. Karpathy et al. extends the connectivity of CNN models over time. Additionally, multi-resolution techniques are utilized to accelerate the training process, effectively reducing the impact of spatio-temporal redundancy on model efficiency in the video modality [27].

The point cloud modality captures information about the position, shape, colour, texture, and other aspects of three-dimensional objects. C. R. Qi et al. introduced the classic PointNet [1] for the point cloud modality, emphasizing the importance of invariance through point data permutation and the significance of global and local features. W. Wu et al.

extended convolution operations to three-dimensional point clouds with the introduction of PointConv [28].

### B. Multimodal Model

While the single-modal methods in Section 2.1 have demonstrated excellent performance within their respective modalities, they often face challenges in generalizing across multiple modalities due to their construction based on specific prior assumptions. Recognizing the intrinsic requirement for intelligent models to utilize multimodal data for geographic object cognition, numerous researchers have endeavoured to balance the cohesion and autonomy among modalities to construct multimodal models.

For joint interpretation of two modalities, H. Li and X.-J. Wu recognized the enhancement possible through fusing RGB and infrared images, which convey information about colour, texture, and temperature. Given the widespread demand and application prospects in military, medical, and other fields, they proposed a dense fusion method for RGB and infrared images: DenseFuse [29]. This method, employing a dense module that connects the outputs of all convolutional layers, successfully achieves pixel-level fusion of the RGB and infrared modalities. A. Sadeghian et al. extended the social GANs [25] and introduced RGB images to enhance scene data in Sophie [30], achieving better results in trajectory prediction tasks. Recognizing the high complementarity between RGB and SAR images, L. H. Hughes et al. proposed a three-step deep neural network framework that utilizes a universal prediction of matching regions, generates heatmaps, and eliminates outliers to match RGB and SAR images [31]. X. Li et al. introduced the DTCND [32], a model that employs a GAN network to migrate RGB and SAR images to the same feature space, facilitating target detection. J. Yang et al. proposed a dual-stream convolutional network that uses high-resolution multispectral images to enhance the spatial resolution of hyperspectral images [33].

Notably, CLIP [5], proposed by A. Radford et al., associates the RGB modality with the text modality using contrastive learning. With pretraining guided by weak supervisory signals from text, CLIP has demonstrated outstanding capabilities in both visual single-modal tasks and visual-language multimodal tasks, inspiring a series of subsequent works [6]–[9]. Y. Zhang et al. introduced a meta-transformer [34], leveraging the contrastive learning paradigm from CLIP to pretrain a universal backbone network under the visual-language modality. It exhibits multimodal generalization abilities across various modalities, such as point clouds, infrared, and hyperspectral data. J. Han et al. directly employed a multimodal large language model as a universal backbone network, proposing the One-LLM, which successfully unifies eight modalities, namely, images, audio, videos, and points [35]. The success of these approaches implies the unique role of language modalities in multimodal models.

Therefore, building upon the aforementioned efforts, we systematically propose the fundamental principle of the LaRF. Guided by this principle, we balance cohesion and autonomy among diverse modalities and introduce a general intelligent

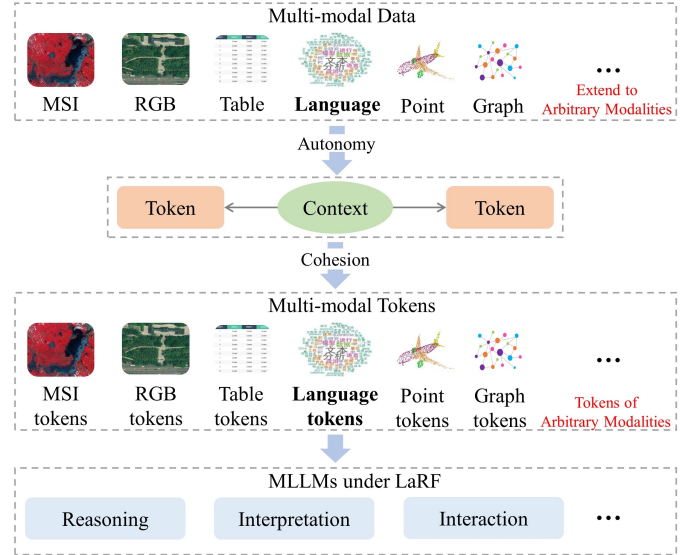


Fig. 2. Guided by the LaRF principle, multimodal data are transformed into a token-context structure similar to language under their respective prior assumptions while maintaining the autonomy of the multimodalities and achieving cohesion among modalities, thus enabling interpretation of multimodal data in the unified language representation space.

model named AllSpark, which unifies thirteen spatio-temporal modalities and possesses the potential to extend to an arbitrary number of modalities.

## III. METHOD

### A. Theory

We observe that in the process of comprehending the world, humans integrate information from multiple modalities, such as hearing, touch, smell, and vision. The concepts formed through the parsing of these modalities ultimately converge in language. Humans engage in associating, reasoning, and expressive behaviours through language. In other words, language precisely encodes human perception and understanding of the world, providing clear definitions and meanings to abstract concepts from each modality.

Inspired by our observation, to balance cohesion and autonomy among multiple modalities, we introduce the fundamental principle of **Language as Reference Framework (LaRF)**.

In terms of the cohesion of multimodalities, the high heterogeneity between multiple spatio-temporal modalities is a major challenge, while the LaRF principle defines the alignment anchor between multimodalities as language explicitly. As shown in Figure 2, we observe that language is encoded by tokens and their contexts, and this structure can be extended to most spatio-temporal modalities. Therefore, we can align highly heterogeneous spatio-temporal modalities to language modalities in structure and semantics, enabling multimodal interpretation in the unified representation space of language. In addition, the important guiding role of natural language prompts is also one of the reasons why the LaRF principle can achieve cohesion among modalities.

In contrast, we can independently encode multiple spatio-temporal modalities into token sequences under their respective prior assumptions, so the LaRF principle does not lead to

the loss of modal autonomy. More importantly, LaRF is not dependent on specific modalities; therefore, theoretically, as long as token representations of modalities can be obtained, the multimodal model guided by LaRF can be extended to arbitrary modalities.

In summary, the significance of LaRF is as follows:

- 1) **Alignment Capability:** Language can accurately encode both cohesion and autonomy information across multiple modalities. Aligning each modality with the language modality enables a unified representation in the same feature space, addressing the challenge of high heterogeneity among modalities.
- 2) **Reasoning Capability:** Language, as a tool for human thought and expression, inherently possesses the ability to perform complex reasoning. Each modality, when represented in a unified space with LaRF, inherits the reasoning capability of language, unlocking the potential for multimodal joint reasoning.
- 3) **Interpretability:** Deep learning methods have long been characterized as opaque "black boxes." However, a multimodal intelligent system constructed based on the LaRF can directly leverage language as a tool. This facilitates the output of interpretable reasoning chains that humans can understand, thereby achieving true explainable artificial intelligence.
- 4) **Interactivity:** Language not only aids humans in understanding intelligent models but also facilitates intelligent models in understanding humans. In an intelligent system guided by the LaRF, humans can directly express their needs using natural language. This iterative correction of the model's output based on human interaction will become a new paradigm for the training and inference of intelligent models.
- 5) **Scalability:** The multimodal system guided by the LaRF is agnostic to specific modalities. New modalities need to establish a mapping to the language model only to participate in joint reasoning with other modalities. Therefore, theoretically, a multimodal model based on LaRF can be extended to an arbitrary number of modalities.

## B. Overview

Guided by the principles mentioned above, the AllSpark we proposed consists of five modules: the modal encoder, modal bridge, text tokenizer, multimodal large language model, and task head. The overall architecture is depicted in Figure 3.

To maintain autonomy among modalities, we designed modality-specific encoders to encode highly heterogeneous data into modality-independent tokens (for details, see Section III-C). However, the dimensions of tokens outputted by modal encoders are still inconsistent. To parse in the unified representational space of language, we introduced the modal bridge from the Lynx [10]. The modal bridge aims to project tokens from each modality into the dimension of the multimodal large language model (Section III-D for details). The formalization of this process is as follows:

$$s_i = \Phi(f_i(m_i), q) \quad (1)$$

Here,  $\{m_{RGB}, m_{MSI}, m_{HSI}, \dots, m_i, \dots, m_{Video}\}$  represents inputs from various modalities, where  $m_{RGB}$  represents the RGB modality,  $m_{MSI}$  represents the MSI modality, and so on.  $f_i$  is defined as the modal encoder for the  $m_i$  modality,  $\Phi$  represents the modal bridge, and  $q \in R^{N \times D}$  represents  $N$  learnable vectors of dimension  $D$  in the modality bridge, where  $D$  is set to 4096, representing the dimensionality of the multimodal large language model. The input data  $m_i$  of each modality are mapped to a token sequence  $s_i \in R^{N \times D}$  of the same dimension as the language model. Table I summarizes the main mathematical symbols and their meanings in the model.

To achieve cohesion among modalities, we employ a unified multimodal large language model to parse data from various modalities. The text tokenizer and multimodal large language model in AllSpark are based on the visual-language model Lynx [10]. To extend Lynx to thirteen spatio-temporal modalities, we designed specific text prompts for each modality to guide the model in correctly parsing information from each modality. Additionally, Lynx incorporates several lightweight multimodal adapter layers internally to accommodate multimodal inputs. We continue this design and do not freeze the parameters of the adapter layers during training to enhance the model's adaptability to other spatio-temporal modalities. Finally, we acknowledge that a gap exists between the parsing results of the model and those of the downstream task. Therefore, we design specific task heads for each task to enhance the model's generalization capability.

The entire model  $M$  can be formalized as:

$$M(m_i, p_i) = H_{task}(F(s_i \oplus T(p_i))) \quad (2)$$

where  $p_i$  represents the text prompt of  $m_i$ ,  $T$  denotes the text tokenizer,  $\oplus$  indicates the concatenation operation of text tokens and modality tokens in the sequence,  $F$  represents the multimodal large language model, and  $H_{task}$  signifies the task head.

All the tasks in our experiments are supervised tasks, with  $y$  denoting the labels,  $L$  representing the loss function, and  $\theta$  representing the learnable parameters in our model. The optimization objective of the model can be formalized as follows:

$$\theta_i = \arg \min_{\theta} L(y, M(m_i, p_i); \theta_i) \quad (3)$$

## C. Independent Encoder for Each Modality

The modal encoder aims to encode the raw data of each modality into a token sequence, formalized as  $t_i = f_i(m_i)$ , where  $t_i \in R^{n \times d}$ . We designed different modal encoders for each modality to maintain autonomy among modalities. The following provides individual introductions for each modality:



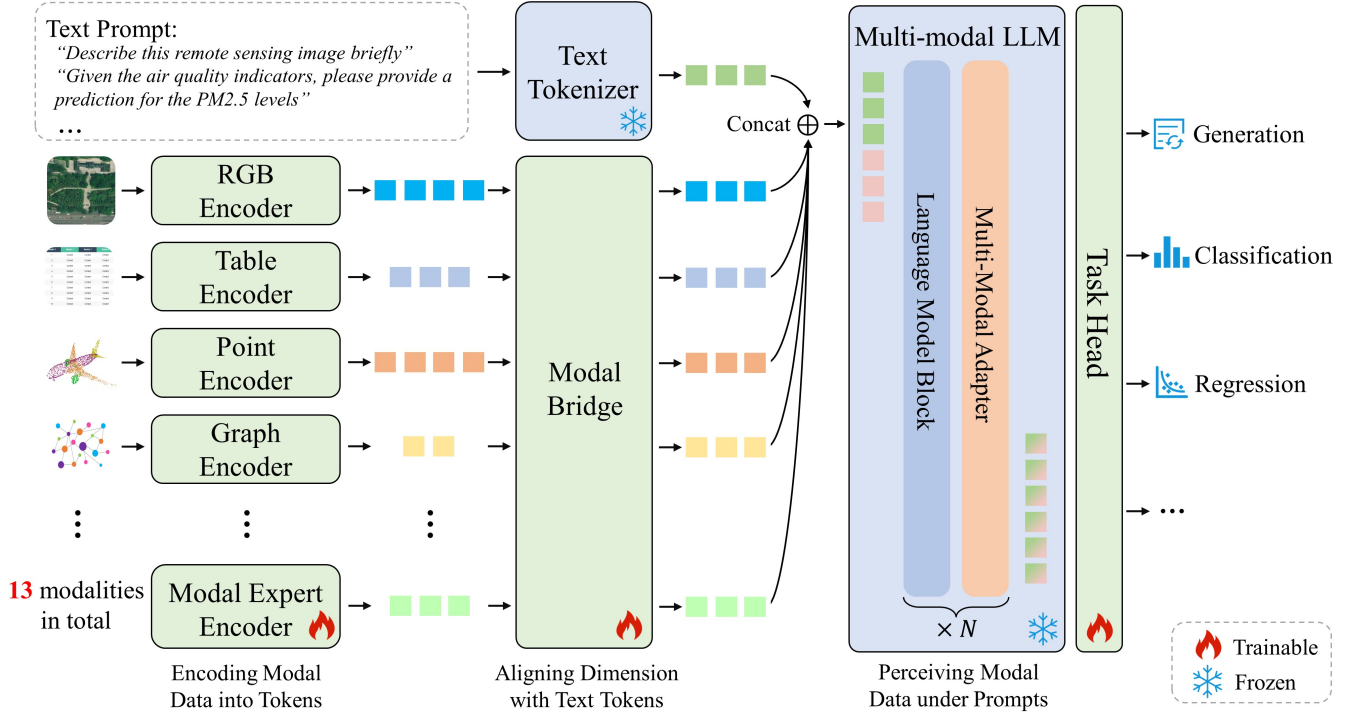


Fig. 3. AllSpark Architecture. Multimodal data are extracted by their respective modal encoders into token sequences. After undergoing dimension alignment with modal-specific text prompt tokens through a modal bridge, the text prompt tokens and modal tokens enter a large language multimodal model for interpretation. Finally, the interpretation result is matched with downstream tasks by task-specific task heads.

TABLE I  
LIST OF SYMBOLS

Module		Variants	
Symbol	Meaning	Symbol	Meaning
$M$	AllSpark	$m_i$	modal $i$
$f_i$	modal encoder for $m_i$	$q$	query vectors of the bridge
$\Phi$	modal bridge	$s_i$	tokens of $m_i$
$T$	text tokenizer	$p_i$	text prompt for $m_i$
$F$	Multimodal LLM	$\theta$	model parameters
$H_{task}$	Task Head	$y$	label
$L$	loss function	$t_i$	tokens of $m_i$
$Enc_n$	$n$ -layer transformer encoders	$W$	weights of the linear layer
$Emb$	embedding layer	$w_i$	word of the code or text
$Enc_{ResNet}$	ResNet		
$Sparse$	sparse module of the TubeViT		
$Grouper$	point grouper of the PointBERT		
$Conv1d$	1D convolution layer		
$FFN$	feedforward network		
$\sigma$	softmax		

#### 1) 1D modal:

**Code & Text:** Code is essentially a specialized form of language, but due to its distinct properties such as having a strict syntax, being unambiguous, and being capable of interacting with machines. we separate it as a distinct modality. Exploring intelligent methods for the code modality is crucial for reliable AI reasoning and achieving interaction between intelligent models and the real world. Since the Lynx model is a language model, we do not design an additional modal encoder for the code and text modalities. Instead, we directly utilize Lynx's text tokenizer, i.e.,  $f(m_{Text/Code}) = T(m_{Text/Code})$ , where

$m_{Text/Code} = \{w_1, w_2, w_3, \dots\}$  represents the sequence of words in the text or code.

#### 2) 2D modal:

**RGB:** RGB imagery represents the visible light spectrum and reflects the electromagnetic characteristics of objects that emit or reflect visible light waves. It is the most common modality used in visual research. RGB imagery is a standard three-band image, i.e.,  $m_{RGB} \in R^{H*W*3}$ . For the modal encoder of this modality, we adopted the visual encoder from the Lynx model: the EVA. The EVA is a large visual backbone model composed of 40 stacked transformer blocks with a

width of 1408. During the experiments, AllSpark loaded the official weights of the EVA model and froze them during training.

**MSI:** Multispectral imagery is a modality extensively studied in the remote sensing field. Typically, it includes more than the three visible light bands present in the RGB modality. MSIs incorporate multiple nonvisible light bands, such as near-infrared, shortwave infrared, coastal atmospheric aerosol, and cirrus bands. Therefore, the number of channels in the imagery is usually greater than the three bands in RGB imagery, i.e.,  $m_{MSI} \in R^{H*W*C}$ , where  $C > 3$ . We extended the PatchEmbed of the standard ViT [18], modifying its channel count to match the number of bands in the input multispectral imagery. This adaptation allows it to serve as the feature encoder for the multispectral modality.

**HSI:** Hyperspectral imagery increases the number of bands compared to multispectral imagery, often reaching hundreds of bands, with each band containing rich information. Unlike RGB and multispectral imagery, where an image serves as a single sample, in hyperspectral imagery, all bands for each pixel are treated as a single sample, i.e.,  $m_{HSI} \in R^{1*1*C}$ . In the modal encoder for hyperspectral imagery, we first use a linear projection layer to expand the feature dimensions for each pixel. This process is formalized as  $W * m_{HSI}^T$ , where  $W \in R^{1*d}$  is the weight matrix of the linear projection layer. Subsequently, we use a 12-layer standard transformer encoder to extract its features. The entire process can be represented as  $f(m_{HSI}) = Enc_{12}(W * m_{HSI}^T)$ .

**Table:** The table modality consists of several rows and columns, where each row represents a record and each column represents a different attribute, i.e.,  $m_{Table} \in R^{row*col}$ . The modal encoder for the table modality inherits the design from TabFormer [36]: first, based on the different degrees of discreteness for each column attribute, we use independent embedding layers to encode discrete and continuous values separately. Subsequently, we employ a single-layer transformer encoder to further extract features. The entire process can be formalized as  $f(m_{Table}) = Enc_1(Emb(m_{Table}))$ .

**Trajectory:** The trajectory modality reflects the changing information of an object over time and space and is composed of a series of two-dimensional coordinate points, i.e.,  $m_{Trajectory} \in R^{l*2}$ , where  $l$  represents the sequence length of trajectory points. The encoder for the trajectory modality inherits the design from TUTR [37]: first, a linear layer is used to expand the dimensions of the two-dimensional trajectory features. This step can be formalized as  $W * m_{Trajectory}$ , where  $W \in R^{d*(l*2)}$  is the weight matrix of the linear projection layer. Then, we use a 2-layer transformer encoder to extract its features. The entire process can be formalized as  $f(m_{Trajectory}) = Enc_2(W * m_{Trajectory})$ .

**SAR:** The synthetic aperture radar (SAR) modality is a type of active remote sensing that reflects the electromagnetic characteristics of objects with respect to microwave backscatter. Due to differences in polarization modes, the final product of SAR imagery is typically a two-band or single-band image, i.e.,  $m_{SAR} \in R^{H*W*2}$ . Therefore, we designed a simple three-layer convolutional network as the modal encoder.

**Infrared:** The dataset we selected for infrared detection

was SYSU-MM01, which is, in fact, a multimodal reidentification dataset comprising both visible and near-infrared (NIR) modalities. The model needs to simultaneously process infrared and visible light images, i.e.,  $m_{Infrared} = \{I_r \in R^{H*W*3}, I_i \in R^{H*W*3}\}$ . We inherited and slightly modified the design of DDAG [38], discarding the parameters of the shared ResNet-50 layers in DDAG and employing two independently parameterized ResNet-50 networks. These networks extract features from infrared and visible light images, and this process can be formalized as  $f(m_{Infrared}) = Enc_{ResNet}(I_r) \oplus Enc_{ResNet}(I_i)$ .

**Graph:** A graph is constructed from a series of nodes and edges, where the attributes of the nodes and the adjacency attributes of the nodes reflect the majority of the features of the graph, i.e.,  $m_{Graph} \in R^{K*d}$ , where  $K$  is the number of nodes and  $d$  is the node feature dimension. In AllSpark, the modality encoder of a graph is based on the STAEformer [39], whose main design idea is to first use a linear layer to extend its feature dimension and then use several embedding layers to separately encode features such as the node's characteristics, spatial characteristics, and temporal characteristics. The entire process can be formalized as  $f(m_{Graph}) = Emb_{node}(W * m_{Graph}^T) \oplus Emb_{spatial}(W * m_{Graph}^T) \oplus Emb_{time}(W * m_{Graph}^T)$ , where  $W \in R^{hidden*d}$  is the weight of the linear layer.

**Oblique Photography:** The oblique photography modality consists of images from multiple views, i.e.,  $m_{Oblique} = \{V_1 \in R^{C*H*W}, V_2 \in R^{C*H*W}, V_3 \in R^{C*H*W}, \dots, V_n \in R^{C*H*W}\}$ , where  $V_i$  represents the image of each view and  $n$  is the number of views. In the encoder for the oblique photography modality, we use the standard ViT model to extract features from multiple view images and concatenate them. The process can be formalized as  $f(m_{Oblique}) = Enc_{12}(V_1) \oplus Enc_{12}(V_2) \oplus Enc_{12}(V_3) \oplus \dots \oplus Enc_{12}(V_n)$ .

### 3) 3D modal:

**Video:** The video modality can be considered as the stacking of images in the temporal dimension, i.e.,  $m_{video} \in R^{T*C*H*W}$ . The significant characteristic of the video modality is its high redundancy in both temporal and spatial dimensions. To address this issue, the encoder for the video modality in AllSpark is based on TubeViT [40], which performs sparse sampling on highly redundant data in both time and space to reduce redundancy. The features obtained from sparse sampling are subsequently fed into a 6-layer transformer encoder for further feature extraction. The process can be formalized as  $f(m_{video}) = Enc_6(Sparse(m_{video}))$ .

**PointClouds:** PointClouds are typically composed of three-dimensional coordinates and feature values  $m_{PointCloud} \in R^{K*(d+3)}$ , where  $K$  represents the number of three-dimensional points and  $d$  represents the dimensionality of the point cloud features, reflecting information such as the spatial position, shape, colour, and texture of objects. The encoder for the point cloud modality inherits the design from PointBERT [41]: first, point cloud data are grouped and encoded to unify the number of points simultaneously inputted. This step can be represented as  $PointGroup = Grouper(m_{PointCloud}) \in R^{G*N*3}$ , where  $G$  represents the number of groups and  $N$  represents the number of points in each group. Next, the

grouped results are input into a one-dimensional convolutional layer to extract feature vectors for each group:  $f_{Group} = \text{Conv1d}(\text{PointGroup}) \in R^{G*d}$ . Finally, the feature vectors for each group are input into a standard 12-layer transformer encoder to extract their global features. The entire process can be formalized as  $f(m_{\text{PointCloud}}) = \text{Enc}_{12}(\text{Conv1d}(\text{Group}(\text{m}_{\text{PointCloud}})))$ .

#### D. Modal2Language Bridge

Although the modal encoders have transformed data from various heterogeneous modalities into a unified token sequence, there are still differences in dimensions between different modal tokens, making it difficult to perceive by a multimodal large language model. The modal bridge, based on the Lynx model, aims to perform dimensional projection from tokens of various modalities to tokens of the language modality. In its implementation, the modal bridge consists of stacked layers, including cross-attention layers and feedforward neural network layers.

In the cross-attention layer, we predefine a learnable query vector  $Q \in R^{N*D}$ , where  $D$  is the internal dimensionality of the language model and  $N$  serves as a hyperparameter that can be flexibly adjusted to accommodate inputs from different modalities. The keys and values in the cross-attention layer are the features outputted by the modal encoders.

The feedforward neural network inherits the classic design from the original transformer and consists of two linear layers with an inserted activation layer. The entire process can be formalized as follows:

$$\Phi(Q, s_i) = \text{FFN} \left( \sigma \left( \frac{QW_q^T (s_i W_k^T)^T}{\sqrt{D}} \right) s_i W_v^T \right) \quad (4)$$

Here,  $W_q \in R^{D*hidden}$ ,  $W_k \in R^{d*hidden}$ , and  $W_v \in R^{d*hidden}$  are the linear projection layer weights defined inside the cross-attention layer for  $Q$ ,  $K$  and  $V$ , respectively.  $\sigma$  denotes the softmax operation.

#### E. Task-Guided Text Prompts and Task Heads

To extend the visual-language multimodal model to thirteen spatio-temporal modalities without intervention from modality expert knowledge, we designed specific text prompts and task heads for each modality and task. Text prompts are used to guide the multimodal language model in correctly interpreting each modality's data, while task heads are employed to match the model's parsing results with specific downstream tasks.

We manually designed one to four specific text prompts for each modality. During the training process, to enhance model performance, we employed a strategy of diversifying prompts, randomly selecting one prompt for each forward pass. However, during testing, for the sake of result stability and reproducibility, the prompt was fixed to be the first prompt among all prompts. Table XVI provides a list of all the text prompts.

Additionally, we noticed that there is still a gap between the multimodal language model's parsing results and the specific

downstream tasks. To enhance the model's generalization capability on downstream tasks, we designed specific task heads for each task. Moreover, to ensure the transferability of modalities across different tasks, the design principle for task heads is to be as simple and lightweight as possible. A detailed summary of each modality's task heads can be found in Table 4.

For classification tasks or downstream tasks that can be formalized as classification tasks, we uniformly use a simple single-layer linear layer as the task head. For instance, we implemented standard classification tasks on the RGB, MSI, SAR, video, and PointCloud modalities. Although the task involving the HSI modality is segmentation, it can be formalized as a per-pixel classification task. Similarly, the reidentification task in the infrared modality can also be formalized as a classification task. Therefore, a single-layer linear layer is used as the task head for the mentioned modalities.

For regression tasks on the table, trajectory, and graph modalities, we also use a linear layer to perform regression predictions. The only difference from classification tasks is the addition of an unscaled operation without learnable parameters. Since the Lynx model itself is a language model, the code and text modalities directly use its native text decoder. The task head for the oblique photography modality is based on the 3D reconstruction architecture from the Ada-MVS [42] model.

## IV. EXPERIMENT

### A. Setup

Our experiments evaluated the adaptability of AllSpark to various spatio-temporal modalities. To provide a realistic evaluation of its multimodal adaptability and facilitate comparisons with existing work in the field, we followed the principles of simplicity, reproducibility, and choosing datasets and tasks that have been widely studied in the domain. The specific details on dataset selection can be found in Section IV-B.

Additionally, for reproducibility, we employed similar experimental settings across all modalities. We used the AdamW optimizer with a learning rate schedule based on cosine annealing. The hyperparameters were adjusted slightly in terms of training epochs and learning rates for different experiments. Table II summarizes the hyperparameter settings for the experiments on each modality.

### B. Dataset

Table 4 summarizes the data and tasks used in the experiments for each modality. Below, we will provide detailed explanations in order:

**Text:** The IMDB [43] dataset is a binary sentiment analysis dataset consisting of 50,000 reviews from the Internet Movie Database (IMDb) labelled as positive or negative. Additionally, the dataset includes some unlabelled data. In our experiments, only the labelled data from the IMDB dataset were utilized for supervised sentiment classification tasks.

**Code:** CodeSearchNet [44] is a large-scale dataset of function code and its documentation from GitHub that covers six



TABLE II  
SUMMARY OF HYPERPARAMETERS

Dimension	Modal	Max Lr	Max Epochs	Warm-up Epochs
1D	Text	$9.0 \times 10^6$	5	1
	Code	$1.0 \times 10^5$	4	1
2D	RGB	$5.0 \times 10^5$	50	5
	MSI	$2.0 \times 10^5$	50	5
	HSI	$1.0 \times 10^4$	30	3
	Infrared	$5.0 \times 10^5$	50	5
	SAR	$9.0 \times 10^6$	30	3
	Oblique Photography	$5.0 \times 10^5$	30	3
	Table	$2.0 \times 10^5$	30	3
	Trajectory	$1.0 \times 10^5$	30	5
	Graph	$8.0 \times 10^5$	10	2
3D	PointCloud	$3.0 \times 10^5$	100	10
	Video	$1.0 \times 10^5$	3	1

programming languages: Go, Java, JavaScript, PHP, Python, and Ruby. The task performed on the code modality is code document generation, and we tested it on the Ruby and JavaScript.

RGB: NWPU-RESISC45 [45] is a large-scale open dataset for visible light remote sensing image scene classification. The dataset included 45 land use categories, such as airplanes, baseball diamonds, beaches, and commercial areas. Each category included 700 remote sensing images, for a total of 31,500 images. The image size is 256\*256 pixels, and we selected a version of the dataset split by the official release using 20% of the data for training.

MSI: The EuroSAT [46] dataset is a multispectral dataset for land use and land cover (LULC) classification. The samples are sourced from the Sentinel-2 optical satellite and include all 13 bands. The data are categorized into 10 classes for a total of 27,000 images. We adopted a random 9:1 split for training and testing.

HSI: The Pavia University dataset is a high-spatial-resolution hyperspectral dataset acquired by the ROSIS sensor. It comprises 103 bands with a size of 610\*340 pixels. The dataset includes nine land cover categories, such as asphalt, meadows, and gravel. We used a 4:6 split for training and testing.

Table: The PRSA [47] dataset is a collection of air quality data from multiple stations in Beijing that contains hourly measurements of air pollutants. The data spans from March 1, 2013, to February 28, 2017, across 12 monitoring stations. In our experiments, we used various features, including time, station information, 4 air pollutant variables (SO<sub>2</sub>, NO<sub>2</sub>, CO, and O<sub>3</sub>), and 6 meteorological variables (temperature, pressure, dew point temperature, amount of precipitation, wind speed, and wind direction). The task was to predict the concentration of PM<sub>2.5</sub>. We split the data into training (40%) and testing sets.

Trajectory: The ETH-UCY [48], [49] dataset is a widely used benchmark for pedestrian trajectory prediction and is

divided into five subsets: ETH, HOTEL, UNIV, ZARA1, and ZARA2. In our experiments, we utilized the ETH subset.

SAR: The MSTAR [50] dataset is a synthetic aperture radar dataset designed for military stationary target recognition that comprises ten categories of military targets. We employed the standard operating conditions (SOCs) dataset preprocessing method proposed by S. Chen et al. [22], ensuring that the serial numbers and target configurations are consistent between the test and training sets while the aspects and depression angles differ.

Infrared: SYSU-MM01 [51] is a cross-modal human reidentification dataset with optical-infrared modalities that includes images from 4 RGB cameras and 2 infrared cameras of 491 different individuals. We adopted the official dataset split, with the training set containing 20,284 RGB images and 9,929 infrared images from 296 individuals and the test set consisting of 3,803 infrared images from 96 individuals used as queries and 301 randomly selected RGB images for reidentification targets.

Graph: METR-LA is a traffic dataset collected from loop detectors on the Los Angeles highways spanning from March 1, 2012, to June 30, 2012. The task is traffic flow prediction.

Oblique Photography: WHU-OMVS [42] is an oblique photography dataset designed for 3D reconstruction tasks. The dataset provides imagery from five different viewpoints, along with camera parameters and other relevant information. It consists of six areas, and in our experiments, area 1 is used as the training set, and area 2 is used as the test set.

Video: The UCF101 [52] dataset is a human action recognition dataset comprising 101 action classes with a total of 13,320 video clips. The videos have a combined duration of 27 hours and a resolution of 320\*240 pixels and were sourced from YouTube.

PointCloud: ModelNet40 [53] is a synthetic point cloud dataset consisting of 40 object categories and a total of 12,311 point cloud objects. We follow the official dataset split, with 9,843 objects used for training and 2,468 for testing.

### C. Results

TABLE III  
RGB IMAGE CLASSIFICATION WITH ALLSPARK

Method	Publication	Acc(%)
CNN-CapsNet [54]	RS2019	89.03
DFAGCN [55]	TNNLS2021	89.29
D-CNN with GoogleNet [56]	TGRS2018	90.49
D-CNN with VGGNet [56]	TGRS2018	91.89
SCCov [57]	TNNLS2019	92.1
SeCo-ResNet-50 [58]	ICCV2021	92.91
MG-CAP [59]	TIP2020	92.95
LSENet [60]	TIP2021	93.34
MSANet [61]	JSTARS2021	93.52
IDCCP [62]	TGRS2021	93.76
MBLANet [63]	TIP2021	94.66
GRMANet-ResNet-50 [64]	TGRS2021	94.72
EMSNNet [65]	TGRS2023	95.37
ViTAE-B + RVSA [66]	TGRS2022	<b>95.69</b>
AllSpark	ours	94.85

1) *RGB*: We evaluated the performance of AllSpark on the RGB image scene classification task using the NWPU-RESISC45 dataset, with the top-1 accuracy as the evaluation metric. AllSpark leverages expert knowledge from Lynx by loading its pretrained weights. Therefore, in Table III, we compare AllSpark with the state-of-the-art models known on the NWPU-RESISC45 dataset. The results indicate that AllSpark outperforms most baseline models, with a margin of only 0.84 compared to that of the SOTA (95.69). This highlights AllSpark’s exceptional perception and interpretation capabilities in the RGB modality.

2) *MSI*: We evaluated the performance of AllSpark on the MSI scene classification task using the EuroSAT dataset. In the experiment, all 13 spectral bands of the images were simultaneously input into the model. The model’s objective was to correctly classify the images into one of the 10 specified categories, and the evaluation metric chosen was the top-1 accuracy. AllSpark does not possess expert knowledge in the multispectral modality, so we categorize the baseline models into two groups, as shown in Table IV: those with expert knowledge intervention and those without. Expert knowledge intervention refers to baseline models pretraining on large datasets such as BigEarthNet and then fine-tuning on the EuroSAT dataset, while no expert knowledge indicates baseline models trained directly from scratch on the EuroSAT dataset. The results show that our model outperforms most models in the no expert knowledge group, with a margin of only 2.60 compared to the state-of-the-art model (ResNet-152). Furthermore, AllSpark lags behind the best result in the expert knowledge group by only 4.75, demonstrating its excellent adaptability to the multispectral modality.

3) *HSI*: We conducted a pixel classification task on the Pavia University dataset for the hyperspectral modality. The model treats all spectral bands of a single pixel as one sample and predicts the land cover category of that pixel. The reported metrics include overall accuracy (OA), average accuracy (AA), and kappa. Since AllSpark does not possess expert knowledge of the hyperspectral modality, we compared it with the semisupervised baselines summarized by D. Uchaev

TABLE IV  
MSI LAND COVER CLASSIFICATION WITH ALLSPARK

Expert Know.	Method	Publication	Acc(%)
No	ResNet-18 [58]	ICCV2021	63.21
	ResNet-50 [67]	IGARSS2023	91.13
	InceptionNet [68]	ICIP2020	93.07
	EfficientNet [69]	IJSTARS2021	93.94
	<b>AllSpark</b>	<b>ours</b>	<b>94.03</b>
Yes	ResNet-152 [67]	IGARSS2023	<b>96.63</b>
	MoCoV2 [58]	ICCV2021	89.51
	SeCo [58]	ICCV2021	93.14
	SEER [70]	Arxiv2022	97.6
	DINO-MC [71]	Arxiv2023	<b>98.78</b>

and D. Uchaev [72]. The results in Table V demonstrate that AllSpark outperforms many hyperspectral image classification methods, such as IFRF and S-DMM, by a factor of 6.42 compared to the best result in terms of OA, highlighting AllSpark’s superior adaptability to the hyperspectral modality.

TABLE V  
HSI PIXEL CLASSIFICATION WITH ALLSPARK

Method	OA	AA	Kappa
3D-CNN	75.24	80.26	68.34
CA-GAN	76.81	76.94	71.02
3D VS-CNN	81.63	83.86	76.46
RPNNet	84.92	83.26	80.52
S-DMM	88.3	93.76	84.9
IFRF	88.38	85.99	84.97
<b>AllSpark</b>	<b>89.18</b>	<b>86.65</b>	<b>85.32</b>
DCFSL	90.71	90.2	87.73
TC-GAN	93.2	91.6	91
PRNet-RF	<b>95.6</b>	<b>94.96</b>	<b>94.27</b>

4) *Table*: For the table modality, we evaluated AllSpark on the regression prediction task using the PRSA [47] dataset. The task involves predicting the concentration of PM2.5 in the air using features such as time, site, 4 air pollutants, and 6 meteorological variables (as detailed in Section IV-B). The performance metrics include the root mean squared error (RMSE), mean absolute error (MAE), and R-squared (R2).

TABLE VI  
PM2.5 PREDICTION WITH ALLSPARK

Expert Arch.	Method	PM2.5		
		RMSE	MAE	R2
<b>No</b>	GWO [73]	62.2	40.8	-
	TabBERT [36]	32.8	-	-
	<b>AllSpark</b>	<b>29.03</b>	<b>18.04</b>	<b>0.87</b>
<b>Yes</b>	Stacked ResNet-LSTM [74]	40.68	23.75	0.8
	CBAM-CNN-Bi-LSTM [75]	<b>18.9</b>	<b>11.2</b>	<b>0.94</b>

Table VI presents the comparative results between AllSpark and the baselines. It is worth noting that some works specifically focus on the prediction task on the PRSA dataset and design expert models with specific architectures based on dataset characteristics. For example, the CBAM-CNN-Bi-LSTM proposed by D. Li et al. [75] used a CNN to extract spatial dependencies between air monitoring stations

and Bi-LSTM to capture the temporal dependencies of PM2.5 data. Similarly, the stacked ResNet-LSTM model proposed by X. Cheng et al. [74] employs a stacking LSTM strategy to enhance the extraction of temporal features in PM2.5 data. Therefore, we categorize baseline methods into two types: those with an expert architecture and those without an expert architecture. Among the models without expert architecture, our approach achieves the best performance among the baselines and is slightly inferior to the state-of-the-art method for models with expert architecture (CBAM-CNN-Bi-LSTM). This reflects the excellent adaptability of AllSpark to the table modality.

5) *Code*: For the code modality, we evaluated the performance of AllSpark on the code document generation task using the CodeSearchNet dataset. This task involves generating corresponding documents based on the provided function code. We conducted tests for both the Ruby and JavaScript languages using the mean reciprocal rank (MRR) [76] as the evaluation metric.

TABLE VII  
CODE DOCUMENT GENERATION WITH ALLSPARK

Expert Know.	Method	MRR	
		Ruby	Javascript
No	BIRNN[68]	0.084	0.153
	ID-CNN[68]	0.245	0.352
	selfAtt[68]	0.365	0.451
	NBoW[68]	0.429	0.461
	RoBERTa[67]	0.625	0.606
	<b>AllSpark</b>	<b>0.627</b>	<b>0.635</b>
Yes	RoBERTa(Code)[67]	0.661	0.64
	CodeBERT[67]	0.693	0.706
	GraphCodeBERT[67]	<b>0.732</b>	<b>0.711</b>

Like in the previous modalities, since MSI-AGI does not possess expert knowledge of the code modality, we categorized the baselines into two groups: those with and without expert knowledge. As shown in Table VII, AllSpark achieved SOTA results in the group without expert knowledge, and the results were comparable to those of models trained with expert knowledge. This finding demonstrates the strong adaptability of AllSpark to the code modality.

6) *PointCloud*: For the PointCloud modality, we evaluated the performance of AllSpark on the ModelNet40 dataset for the classification task, with the top-1 accuracy as the metric. In the context of single-modal studies focused on point clouds, we observed that due to the unique three-dimensional structure of point cloud data, most works concentrate on designing specific structures to maintain properties such as permutation invariance and symmetry in 3D point clouds. However, these structures designed for the unique priors of the modality are challenging to transfer across modalities. Additionally, some methods tend to pretrain on large point cloud datasets to acquire general modal expert knowledge before generalizing to specific downstream tasks to improve performance.

The AllSpark module is designed based on a general sequence-to-sequence architecture. As shown in Table VIII, in the absence of both modality expert architectural designs and modal expert knowledge, AllSpark still outperforms classical

TABLE VIII  
POINTCLOUD CLASSIFICATION WITH ALLSPARK

Method	Expert Architecture	Expert Knowledge	Acc(%)
PointNet [1]	Yes	No	89.2
Kd-net [77]	Yes	No	90.6
SPH3D-GCN [78]	Yes	No	91.4
PointNet++ [79]	Yes	No	91.9
SO-Net [80]	Yes	No	92.5
PointVGG [81]	Yes	No	93.6
PointBERT [41]	No	Yes	93.8
PointGPT [82]	Yes	Yes	<b>94.9</b>
AllSpark	<b>No</b>	<b>No</b>	91.2

networks with point cloud-specific structures (PointNet, Kd-Net). This approach maintains comparability with the state-of-the-art PointGPT model, which has both a modal expert structure and modal expert knowledge. This finding suggested that AllSpark has significant potential for applications in the point cloud modality.

7) *Trajectory*: For the trajectory modality, we evaluated the performance of AllSpark on the ETH dataset in the trajectory prediction task. This task involves predicting possible two-dimensional trajectories based on a set of two-dimensional coordinate points within a certain time period. We report accuracy using the average displacement error (ADE) and final displacement error (FDE) [37]. Given the future trajectory  $\{x_t, y_t\}_{t=T_{bos}+1}^T$  (ground truth) and the predicted trajectory  $\{\hat{x}_t, \hat{y}_t\}_{t=T_{bos}+1}^T$ , the ADE and FDE are used to measure their  $L2$  distances, calculated as follows:

$$ADE = \frac{1}{T_{pred}} \sum_{t=T_{bos}}^T \sqrt{(x_t - \hat{x}_t)^2 + (y_t - \hat{y}_t)^2} \quad (5)$$

$$FDE = \sqrt{(x_T - \hat{x}_T)^2 + (y_T - \hat{y}_T)^2} \quad (6)$$

In Table IX, AllSpark is compared with the state-of-the-art trajectory prediction models. The results indicate that AllSpark, which uses a unified structure without trajectory modality expert knowledge, outperforms most expert models. It achieves a prediction accuracy close to that of the SOTA model (STAR), with a difference of only 0.07 in the ADE metric and 0.11 in the FDE metric. This finding suggested that AllSpark demonstrated excellent adaptability to the trajectory modality.

8) *SAR*: For the SAR modality, the adaptability of AllSpark was tested on the MSTAR dataset, where the model is required to identify SAR images of ten military targets, and the metric used is the top-1 accuracy. In the experiment, the preprocessing of the MSTAR dataset followed the SOC settings from AConvNets [22]. Table X presents the comparison results between AllSpark and the state-of-the-art model under these settings. Since AllSpark lacks expert knowledge of SAR image modalities and spatial invariance prior to changes in perspective; its performance on the MSTAR dataset is suboptimal, with an accuracy of 88%. This approach is comparable to the EMACH method. Enhancing the model's adaptability to SAR images

TABLE IX  
TRAJECTORY PREDICTION WITH ALLSPARK

Method	ADE/FDE
Social GAN	0.87/1.62
SoPhie	0.70/1.43
STAR	<b>0.36/0.64</b>
SGCN	0.63/1.03
CAGN	0.41/0.65
SIT	0.39/0.62
SocialVAE	0.47/0.76
PCENet	0.54/0.87
AgentFormer	0.45/0.75
MemoNet	0.40/0.61
SocialVAE+FPC	0.41/ <b>0.58</b>
TUTR	0.40/0.61
AllSpark	0.43/0.69

and improving its ability to extract spatial information are directions for future research.

TABLE X  
SAR CLASSIFICATION WITH ALLSPARK

Method	Acc(%)
EMACH [83]	88
SVM [83]	90
AdaBoost [83]	92
MSRC [84]	93.6
IGT [83]	95
MSS [85]	96.6
Cond Gauss [86]	97
M-PMC [87]	98.8
AConvNets [22]	<b>99.13</b>
AllSpark	88

9) *Infrared*: AllSpark’s adaptability to the infrared modality was tested on the SYSU-MM01 dataset in a cross-modal human reidentification task involving RGB and infrared modalities. In this experiment, the model receives both an infrared image and an RGB image and is tasked with identifying and matching the same person across different modality images. Table XI compares AllSpark and the other state-of-the-art reidentification methods, with the evaluation metric being rank at an accuracy of 20. The results indicate that AllSpark (76.31%) achieved similar accuracy to that of HSME (77.95%). While our method did not reach the highest accuracy, it surpassed some expert models in RGB-infrared reidentification (e.g., TONE, HCML) when using a unified architecture without modal expert knowledge, demonstrating the potential of AllSpark in handling the infrared modality.

10) *Graph*: For the graph modality, the performance of AllSpark was evaluated on the traffic flow prediction task using the METR-LA dataset. The evaluation metrics include the RMSE, MAE, and R2. Table XII compares AllSpark and the state-of-the-art methods on the METR-LA dataset, with the baseline derived from [39]. The results show that AllSpark, without the intervention of modal expert knowledge, is only 0.47 away from the best result in terms of the RMSE, demonstrating its excellent adaptability to the graph modality.

11) *Language*: We tested AllSpark’s natural language processing capabilities on the IMDB dataset [43] with the task of

TABLE XI  
VISIBLE-INFRARED REIDENTIFICATION WITH ALLSPARK

Method	Rank-20(All-search)
Two-stream [51]	65.5
One-stream [51]	66.74
TONE [88]	68.6
HCML [88]	69.17
Zero-Pad [51]	71.33
<b>AllSpark</b>	<b>76.31</b>
HSME [89]	77.95
BDTR [90]	81.07
DDAG [38]	<b>95.81</b>

TABLE XII  
TRAFFIC PREDICTION WITH ALLSPARK

Method	RMSE	MAE	R2
HI	6.8	14.2	10.15
GWNet	3.51	7.28	9.96
DCRNN	3.54	7.47	10.32
AGCRN	3.59	7.45	10.47
STGCN	3.6	7.43	10.35
GTS	3.59	7.44	10.25
MTGNN	3.47	7.21	9.7
STNorm	3.57	7.51	10.24
GMAN	3.44	7.35	10.07
PDFormer	3.62	7.47	10.91
STID	3.55	7.55	10.95
STAEformer	<b>3.34</b>	<b>7.02</b>	<b>9.7</b>
AllSpark	3.81	7.52	11.24

binary sentiment classification (positive or negative). AllSpark loads weights from the Lynx; therefore, it can be considered to possess expert knowledge in the natural language modality. Compared with the SOTA models on the IMDB dataset, as shown in Table XIII, AllSpark outperformed most language models, with only a 0.32 difference from the SOTA result. This highlights AllSpark’s powerful understanding and analysis capabilities in natural language.

TABLE XIII  
TEXT UNDERSTANDING WITH ALLSPARK

Method	Acc(%)
RoBERTa [91]	95.3
ULMFiT [92]	95.4
BERT [93]	95.49
Mixed VAT [94], [95]	95.68
LongFormer [96]	95.7
XLNet [97]	96.8
ERNIE-Doc-Large [98]	<b>97.1</b>
AllSpark	96.78

12) *Video*: For the video modality, we evaluated AllSpark’s performance on action recognition tasks using the UCF101 dataset. The model is tasked with understanding videos and accurately classifying them into one of the 101 classes, with the evaluation metric being the top-1 accuracy. In Table XIV, we compare AllSpark with the current state-of-the-art models. Currently, AllSpark’s adaptation to the video modality is not optimal, as it shows a significant difference from the baseline model results. We attribute this to two main reasons:

1. The high redundancy in video information increases the training cost for AllSpark. We trained it for only 3 epochs on the UCF101 dataset. 2. AllSpark’s model architecture lacks flexibility for three-dimensional data, making it less effective at capturing temporal information.

TABLE XIV  
VIDEO CLASSIFICATION WITH ALLSPARK

Method	Acc(%)
OPN	59.6
VCOP	72.4
SpeedNet	81.1
VTHCL	82.1
CVRL	94.4
VideoMAE v1	96.1
VideoMAE v2	99.6
AllSpark	27.5

13) *Oblique Photography*: For the oblique photography modality, we tested AllSpark’s performance on the 3D reconstruction task using the WHU-OMVS dataset. The model takes five-view images as input, and the goal is to output depth maps for reconstructing 3D models. The evaluation metric used was the percentage of accurate grids in total (PAG) [42], calculated by the following formula:

$$PAG_a = \left( \frac{m_a}{m} \right) * 100 \quad (7)$$

The suffixes in the PAG represent different accuracy standards, where  $PAG_6$  signifies an error within 0.6 metres and  $PAG_{10}$  indicates an error within 1 metre. Table XV compares AllSpark with popular multiview 3D reconstruction models on the WHU-OMVS dataset. AllSpark falls short in terms of accuracy compared to modality-specific expert models. We speculate two possible reasons: 1. Dense spatial information gradually diminishes in the deep structure of large models, a point verified in our exploratory experiments involving segmentation, detection, etc.; 2. The model architecture lacks flexibility and cannot connect gradual features like expert 3D reconstruction models such as Ada-MVS. Additionally, these methods lack the ability to design specific model structures for processing, severely restricting their performance. Adapting multimodal large models to dense prediction tasks and optimizing the architecture are future research directions.

TABLE XV  
3D RECONSTRUCTION WITH ALLSPARK

Method	$PAG_6$	$PAG_{10}$
MVSNet	81.15	91.44
CasMVSNet	95.45	98.02
Ada-MVS	96.14	98.1
UCSNet	96.25	98.45
AllSpark	6.4	10.4

## V. DISCUSSION

### A. Limitations

Certainly, our work has several limitations, which will guide our future research directions:

- 1) **Lack of interaction between different modalities.** While AllSpark incorporates interactions between infrared and RGB modalities, for other modalities, it essentially uses a unified model for multiple single-modal tasks. This is primarily due to constraints such as the lack of multimodal paired data, the inflexibility of the model architecture, and the limited richness of multimodal interaction tasks. In the future, we plan to explore and work more extensively in these directions.
- 2) **There is a lack of in-depth research on multimodal alignment methods.** While we introduced the basic principles of the LaRF and aligned all the modalities to the language modality, our approach included only introducing the modality bridge from Lynx as the alignment method. We have not conducted in-depth research into the various methods of multimodal alignment. Moreover, our testing focused on the model’s adaptability to different modalities, and we have not explored potential capabilities such as interactive reasoning, zero-shot learning, or multimodal emergence that the model may possess after alignment with language. In the future, we plan to delve deeper into researching multimodal alignment methods, and we will design additional tasks and experiments to explore and reveal the upper limits and boundaries of large model reasoning capabilities.
- 3) **Initial work.** Our current work is still in its initial exploratory phase, and we have not carefully refined AllSpark’s adaptability and performance on each modality. As a result, the model exhibits suboptimal performance on certain imaging modalities, such as oblique photography, SAR, and video. In the future, we plan to conduct more refined and targeted adjustments for each modality to enhance overall performance.
- 4) **Expensive cost:** Multimodal large language models, due to prolonged pretraining, typically possess universal reasoning capabilities in certain modalities. We generalize their applicability to other modalities by utilizing modality bridges to project other modalities onto the language modality. Although we freeze most of the parameters, fine-tuning even once on 2 A6000 GPUs often requires more than a day. Given the increasing training costs for large models, exploring methods to generalize their universal reasoning abilities is one of our future research directions.
- 5) **Interesting phenomenon.** During our exploratory experiments, we discovered several interesting properties of large models. For instance, spatial information tends to degrade in large models, leading to collapse when performing dense prediction tasks such as segmentation and detection. Additionally, these models struggle to optimize when transferred to a small quantity of downstream data. Large models often require smaller hyperparameters and are sensitive to them. These observations might partially reveal the working mechanisms of large models, and we plan to conduct additional in-depth investigations into these phenomena in the future.

### B. Potential of the LaRF

Inspired by the human cognitive system and linguistic philosophy, we propose the "LaRF" as the first principle for constructing our unified multimodal model. Its foreseeable potential includes at least the following three points:

- 1) **Efficient Generalization of Large Models.** Currently, the computational power and data scale required for training large models are rapidly expanding, and even the cost of fine-tuning large models is becoming prohibitive. Therefore, in the future, training large models for every domain will be almost impossible. Language, however, holds the potential for achieving efficient generalization of large models, expanding them from their native domains to additional domains at minimal cost. With our proposed AllSpark, we designed simple text prompts and task heads for each modality, demonstrating significant potential for multimodal expansion. In theory, AllSpark, built on the LaRF principle, can be extended to arbitrary modalities. In the future, we will conduct more in-depth research on the impact of text prompts and lightweight parameter modules on the generalization of large models.
- 2) **Interpretable Reasoning.** Deep learning models have often been referred to as "black boxes," indicating that the reasoning process of these models is invisible and challenging to interpret. Research on the interpretability of deep learning models often relies on complex mathematical models and numerous assumptions, greatly limiting the practical application of deep learning methods in fields such as clinical medicine, military, and national resources where low fault tolerance or high confidentiality are crucial. However, language, as a tool for human thought and communication, provides models based on LaRF with the potential to use natural language directly for outputting reasoning chains and justifications.
- 3) **Transition from an end-to-end to an interactive paradigm.** The end-to-end paradigm refers to the learning approach where the model takes input and directly outputs results. In recent years, the end-to-end paradigm has become increasingly popular due to its simple and clear architecture and excellent performance. However, this approach also has clear disadvantages, such as uncontrollable internal operations, the need to optimize the whole for certain problems, and difficulty in pinpointing the cause of issues. A LaRF-based architecture has the potential to achieve an interactive paradigm in which users input raw data and corresponding text prompts and the model automatically performs relevant operations based on the prompts. Users can even iteratively adjust the text prompts based on the results. Therefore, in terms of both performance and controllability, the interactive paradigm has advantages that are incomparable to those of the end-to-end paradigm.

Inspired by human cognitive systems and linguistic philosophy, we propose that the construction of multimodal models follow the fundamental principle of **Language as Reference Framework (LaRF)**. Guided by this principle, we use language to balance the cohesion and autonomy of modalities, presenting a unified intelligent model, AllSpark, encompassing thirteen spatio-temporal modalities. The experimental results demonstrated that AllSpark exhibited excellent adaptability and application potential across various spatio-temporal modalities, highlighting the feasibility and potential of constructing multimodal models with LaRF. AllSpark remains an initial exploratory work, and in the future, we aim to delve deeper into the mechanisms guided by natural language, the efficient generalization of large models, and the transition to an interactive paradigm.

## VI. CONCLUSION

Leveraging multimodal data is an inherent requirement for intelligent models to achieve geographic object cognition.



## APPENDIX

TABLE XVI: List of prompts

Dimension	Modal	Prompt
1D	Text	1.Please determine if this movie review is positive or negative?
	Code	-
	RGB	1.This remote sensing image belongs to which of the following categories: [Category list of the NWPU dataset] 2.Describe this remote sensing image briefly 3.Find a word that is most relevant to this remote sensing image 4.Describe the key elements in this remote sensing image
	MSI	1.Based on the multi-spectral imagery feature description, please classify this object 2.Given the following multi-spectral imagery characteristics, please output the most fitting scene label
2D	HSI	1.Given the spectral information, can you help determine which class this pixel belongs to? 2.Here is the spectral data for a pixel. Considering the typical characteristics of land cover classes, could you provide a detailed analysis and suggest the most likely class for this pixel? 3.The spectral information for a pixel is given, but the data is noisy. Given the potential variability, which land cover classes should be considered as possible candidates for this pixel?
	Table	1.Please utilize the provided air quality indicators to accurately predict the concentrations of PM2.5 in the atmosphere 2.Given the air quality indicators, please provide a prediction for the PM2.5 levels at this particular moment
	Oblique Photography	1.Please reconstruct the 3D model from the given images of five different views.
	Trajectory	1.Based on their past positions and movements in a crowded environment, predict the future trajectory of a selected pedestrian. 2.Using the pedestrian trajectory data, along with additional information about the surrounding environment, predict the future path of the pedestrian. 3.Given the current and past positions of a pedestrian and their neighboring pedestrians, predict the main pedestrian's trajectory
	SAR	1.Based on the SAR imagery feature description, please classify this object 2.Given the following SAR imagery characteristics, please output the most fitting scene label
	Infrared	1.Given an infrared image of a person, find and highlight the same person in a set of visible light images, paying close attention to features like clothing, posture, and gait 2.Analyze the characteristics of a person in a visible light image, such as clothing texture, color, and body shape. Then, locate the person with matching features in a series of infrared images
	Graph	1.Given the current traffic data including vehicle flow rate, average speed, and time of day from the METRLA dataset, predict the traffic flow 2.Analyze the historical data on vehicle speeds and flow rates from the METRLA dataset for the past week. Identify any patterns or trends and predict the traffic conditions

Dimension	Modal	Prompt
3D	Video	1.Please analyze this video and describe the characteristics of the action in detail 2.Watch this short clip and provide a step-by-step description of the action sequence
	Point Cloud	1.Classify the provided point cloud sample into the correct category 2.Look at the point cloud data characteristics and classify the object 3.Please analyze the given point cloud dataset and determine which category it belongs to. Focus on the shape and structure evident in the point cloud

## REFERENCES

- [1] C. R. Qi, H. Su, K. Mo, and L. J. Guibas, "Pointnet: Deep learning on point sets for 3d classification and segmentation," in *Proceedings of the IEEE conference on computer vision and pattern recognition*, 2017, pp. 652–660.
- [2] A. Vaswani, N. Shazeer, N. Parmar, J. Uszkoreit, L. Jones, A. N. Gomez, L. Kaiser, and I. Polosukhin, "Attention is all you need," *Advances in neural information processing systems*, vol. 30, 2017.
- [3] T. N. Kipf and M. Welling, "Semi-supervised classification with graph convolutional networks," *arXiv preprint arXiv:1609.02907*, 2016.
- [4] S. C. Kulkarni and P. P. Rege, "Pixel level fusion techniques for sar and optical images: A review," *Information Fusion*, vol. 59, pp. 13–29, 2020.
- [5] A. Radford, J. W. Kim, C. Hallacy, A. Ramesh, G. Goh, S. Agarwal, G. Sastry, A. Askell, P. Mishkin, J. Clark *et al.*, "Learning transferable visual models from natural language supervision," in *International conference on machine learning*. PMLR, 2021, pp. 8748–8763.
- [6] J. Lu, D. Batra, D. Parikh, and S. Lee, "Vilbert: Pretraining task-agnostic visiolinguistic representations for vision-and-language tasks," *Advances in neural information processing systems*, vol. 32, 2019.
- [7] W. Kim, B. Son, and I. Kim, "Vilt: Vision-and-language transformer without convolution or region supervision," in *International Conference on Machine Learning*. PMLR, 2021, pp. 5583–5594.
- [8] J.-B. Alayrac, J. Donahue, P. Luc, A. Miech, I. Barr, Y. Hasson, K. Lenc, A. Mensch, K. Millican, M. Reynolds *et al.*, "Flamingo: a visual language model for few-shot learning," *Advances in Neural Information Processing Systems*, vol. 35, pp. 23 716–23 736, 2022.
- [9] J. Li, D. Li, C. Xiong, and S. Hoi, "Blip: Bootstrapping language-image pre-training for unified vision-language understanding and generation," in *International Conference on Machine Learning*. PMLR, 2022, pp. 12 888–12 900.
- [10] Y. Zeng, H. Zhang, J. Zheng, J. Xia, G. Wei, Y. Wei, Y. Zhang, and T. Kong, "What matters in training a gpt4-style language model with multimodal inputs?" *arXiv preprint arXiv:2307.02469*, 2023.
- [11] Z. Feng, D. Guo, D. Tang, N. Duan, X. Feng, M. Gong, L. Shou, B. Qin, T. Liu, D. Jiang *et al.*, "Codebert: A pre-trained model for programming and natural languages," *arXiv preprint arXiv:2002.08155*, 2020.
- [12] J. D. M.-W. C. Kenton and L. K. Toutanova, "Bert: Pre-training of deep bidirectional transformers for language understanding," in *Proceedings of naacL-HLT*, vol. 1, 2019, p. 2.
- [13] A. Radford, K. Narasimhan, T. Salimans, I. Sutskever *et al.*, "Improving language understanding by generative pre-training," 2018.
- [14] A. Radford, J. Wu, R. Child, D. Luan, D. Amodei, I. Sutskever *et al.*, "Language models are unsupervised multitask learners," *OpenAI blog*, vol. 1, no. 8, p. 9, 2019.
- [15] T. Brown, B. Mann, N. Ryder, M. Subbiah, J. D. Kaplan, P. Dhariwal, A. Neelakantan, P. Shyam, G. Sastry, A. Askell *et al.*, "Language models are few-shot learners," *Advances in neural information processing systems*, vol. 33, pp. 1877–1901, 2020.
- [16] J. Achiam, S. Adler, S. Agarwal, L. Ahmad, I. Akkaya, F. L. Aleman, D. Almeida, J. Altschmidt, S. Altman, S. Anadkat *et al.*, "Gpt-4 technical report," *arXiv preprint arXiv:2303.08774*, 2023.
- [17] K. He, X. Zhang, S. Ren, and J. Sun, "Deep residual learning for image recognition," in *Proceedings of the IEEE conference on computer vision and pattern recognition*, 2016, pp. 770–778.
- [18] A. Dosovitskiy, L. Beyer, A. Kolesnikov, D. Weissenborn, X. Zhai, T. Unterthiner, M. Dehghani, M. Minderer, G. Heigold, S. Gelly *et al.*, "An image is worth 16x16 words: Transformers for image recognition at scale," *arXiv preprint arXiv:2010.11929*, 2020.
- [19] B. Huang, B. Zhao, and Y. Song, "Urban land-use mapping using a deep convolutional neural network with high spatial resolution multispectral remote sensing imagery," *Remote Sensing of Environment*, vol. 214, pp. 73–86, 2018.
- [20] X. Yang, Y. Ye, X. Li, R. Y. Lau, X. Zhang, and X. Huang, "Hyperspectral image classification with deep learning models," *IEEE Transactions on Geoscience and Remote Sensing*, vol. 56, no. 9, pp. 5408–5423, 2018.
- [21] H. Chen, A. Chen, L. Xu, H. Xie, H. Qiao, Q. Lin, and K. Cai, "A deep learning cnn architecture applied in smart near-infrared analysis of water pollution for agricultural irrigation resources," *Agricultural Water Management*, vol. 240, p. 106303, 2020.
- [22] S. Chen, H. Wang, F. Xu, and Y.-Q. Jin, "Target classification using the deep convolutional networks for sar images," *IEEE transactions on geoscience and remote sensing*, vol. 54, no. 8, pp. 4806–4817, 2016.
- [23] Y. Yao, Z. Luo, S. Li, T. Fang, and L. Quan, "Mvsnet: Depth inference for unstructured multi-view stereo," in *Proceedings of the European conference on computer vision (ECCV)*, 2018, pp. 767–783.
- [24] S. Ö. Arik and T. Pfister, "Tabnet: Attentive interpretable tabular learning," in *Proceedings of the AAAI conference on artificial intelligence*, vol. 35, no. 8, 2021, pp. 6679–6687.
- [25] A. Gupta, J. Johnson, L. Fei-Fei, S. Savarese, and A. Alahi, "Social gan: Socially acceptable trajectories with generative adversarial networks," in *Proceedings of the IEEE conference on computer vision and pattern recognition*, 2018, pp. 2255–2264.
- [26] P. Veličković, G. Cucurull, A. Casanova, A. Romero, P. Lio, and Y. Bengio, "Graph attention networks," *arXiv preprint arXiv:1710.10903*, 2017.
- [27] A. Karpathy, G. Toderici, S. Shetty, T. Leung, R. Sukthankar, and L. Fei-Fei, "Large-scale video classification with convolutional neural networks," in *Proceedings of the IEEE conference on Computer Vision and Pattern Recognition*, 2014, pp. 1725–1732.
- [28] W. Wu, Z. Qi, and L. Fuxin, "Pointconv: Deep convolutional networks on 3d point clouds," in *Proceedings of the IEEE/CVF Conference on computer vision and pattern recognition*, 2019, pp. 9621–9630.
- [29] H. Li and X.-J. Wu, "Densefuse: A fusion approach to infrared and visible images," *IEEE Transactions on Image Processing*, vol. 28, no. 5, pp. 2614–2623, 2018.
- [30] A. Sadeghian, V. Kosaraju, A. Sadeghian, N. Hirose, H. Rezatofighi, and S. Savarese, "Sophie: An attentive gan for predicting paths compliant to social and physical constraints," in *Proceedings of the IEEE/CVF conference on computer vision and pattern recognition*, 2019, pp. 1349–1358.
- [31] L. H. Hughes, D. Marcos, S. Lobry, D. Tuia, and M. Schmitt, "A deep learning framework for matching of sar and optical imagery," *ISPRS Journal of Photogrammetry and Remote Sensing*, vol. 169, pp. 166–179, 2020.
- [32] X. Li, Z. Du, Y. Huang, and Z. Tan, "A deep translation (gan) based change detection network for optical and sar remote sensing images," *ISPRS Journal of Photogrammetry and Remote Sensing*, vol. 179, pp. 14–34, 2021.
- [33] J. Yang, Y.-Q. Zhao, and J. C.-W. Chan, "Hyperspectral and multispectral image fusion via deep two-branches convolutional neural network," *Remote Sensing*, vol. 10, no. 5, p. 800, 2018.
- [34] Y. Zhang, K. Gong, K. Zhang, H. Li, Y. Qiao, W. Ouyang, and X. Yue, "Meta-transformer: A unified framework for multimodal learning," *arXiv preprint arXiv:2307.10802*, 2023.
- [35] J. Han, K. Gong, Y. Zhang, J. Wang, K. Zhang, D. Lin, Y. Qiao, P. Gao, and X. Yue, "Onellm: One framework to align all modalities with language," *arXiv preprint arXiv:2312.03700*, 2023.
- [36] I. Padhi, Y. Schiff, I. Melnyk, M. Rigotti, Y. Mroueh, P. Dognin, J. Ross, R. Nair, and E. Altman, "Tabular transformers for modeling multivariate time series," in *ICASSP 2021-2021 IEEE International Conference on Acoustics, Speech and Signal Processing (ICASSP)*. IEEE, 2021, pp. 3565–3569.
- [37] L. Shi, L. Wang, S. Zhou, and G. Hua, "Trajectory unified transformer for pedestrian trajectory prediction," in *Proceedings of the IEEE/CVF International Conference on Computer Vision*, 2023, pp. 9675–9684.
- [38] M. Ye, J. Shen, D. J. Crandall, L. Shao, and J. Luo, "Dynamic dual-attentive aggregation learning for visible-infrared person re-identification," in *Computer Vision—ECCV 2020: 16th European Conference, Glasgow, UK, August 23–28, 2020, Proceedings, Part XVII*. Springer, 2020, pp. 229–247.
- [39] H. Liu, Z. Dong, R. Jiang, J. Deng, J. Deng, Q. Chen, and X. Song, "Spatio-temporal adaptive embedding makes vanilla transformer sota for traffic forecasting," in *Proceedings of the 32nd ACM International Conference on Information and Knowledge Management*, 2023, pp. 4125–4129.
- [40] A. Piergiovanni, W. Kuo, and A. Angelova, "Rethinking video vits: Sparse video tubes for joint image and video learning," in *Proceedings of the IEEE/CVF Conference on Computer Vision and Pattern Recognition*, 2023, pp. 2214–2224.
- [41] X. Yu, L. Tang, Y. Rao, T. Huang, J. Zhou, and J. Lu, "Point-bert: Pre-training 3d point cloud transformers with masked point modeling," in *Proceedings of the IEEE/CVF Conference on Computer Vision and Pattern Recognition*, 2022, pp. 19 313–19 322.
- [42] J. Liu, J. Gao, S. Ji, C. Zeng, S. Zhang, and J. Gong, "Deep learning based multi-view stereo matching and 3d scene reconstruction from oblique aerial images," *ISPRS Journal of Photogrammetry and Remote Sensing*, vol. 204, pp. 42–60, 2023.
- [43] A. Maas, R. E. Daly, P. T. Pham, D. Huang, A. Y. Ng, and C. Potts, "Learning word vectors for sentiment analysis," in *Proceedings of the 49th annual meeting of the association for computational linguistics: Human language technologies*, 2011, pp. 142–150.

- [44] H. Husain, H.-H. Wu, T. Gazit, M. Allamanis, and M. Brockschmidt, "Codesearchnet challenge: Evaluating the state of semantic code search," *arXiv preprint arXiv:1909.09436*, 2019.
- [45] G. Cheng, J. Han, and X. Lu, "Remote sensing image scene classification: Benchmark and state of the art," *Proceedings of the IEEE*, vol. 105, no. 10, pp. 1865–1883, 2017.
- [46] P. Helber, B. Bischke, A. Dengel, and D. Borth, "Eurosat: A novel dataset and deep learning benchmark for land use and land cover classification," *IEEE Journal of Selected Topics in Applied Earth Observations and Remote Sensing*, vol. 12, no. 7, pp. 2217–2226, 2019.
- [47] S. Zhang, B. Guo, A. Dong, J. He, Z. Xu, and S. X. Chen, "Cautionary tales on air-quality improvement in beijing," *Proceedings of the Royal Society A: Mathematical, Physical and Engineering Sciences*, vol. 473, no. 2205, p. 20170457, 2017.
- [48] S. Pellegrini, A. Ess, K. Schindler, and L. Van Gool, "You'll never walk alone: Modeling social behavior for multi-target tracking," in *2009 IEEE 12th international conference on computer vision*. IEEE, 2009, pp. 261–268.
- [49] A. Lerner, Y. Chrysanthou, and D. Lischinski, "Crowds by example," in *Computer graphics forum*, vol. 26, no. 3. Wiley Online Library, 2007, pp. 655–664.
- [50] E. R. Keydel, S. W. Lee, and J. T. Moore, "Mstar extended operating conditions: A tutorial," *Algorithms for Synthetic Aperture Radar Imagery III*, vol. 2757, pp. 228–242, 1996.
- [51] A. Wu, W.-S. Zheng, H.-X. Yu, S. Gong, and J. Lai, "Rgb-infrared cross-modality person re-identification," in *Proceedings of the IEEE international conference on computer vision*, 2017, pp. 5380–5389.
- [52] K. Soomro, A. R. Zamir, and M. Shah, "Ucf101: A dataset of 101 human actions classes from videos in the wild," *arXiv preprint arXiv:1212.0402*, 2012.
- [53] Z. Wu, S. Song, A. Khosla, F. Yu, L. Zhang, X. Tang, and J. Xiao, "3d shapenets: A deep representation for volumetric shapes," in *Proceedings of the IEEE conference on computer vision and pattern recognition*, 2015, pp. 1912–1920.
- [54] W. Zhang, P. Tang, and L. Zhao, "Remote sensing image scene classification using cnn-capsnet," *Remote Sensing*, vol. 11, no. 5, p. 494, 2019.
- [55] K. Xu, H. Huang, P. Deng, and Y. Li, "Deep feature aggregation framework driven by graph convolutional network for scene classification in remote sensing," *IEEE Transactions on Neural Networks and Learning Systems*, vol. 33, no. 10, pp. 5751–5765, 2021.
- [56] G. Cheng, C. Yang, X. Yao, L. Guo, and J. Han, "When deep learning meets metric learning: Remote sensing image scene classification via learning discriminative cnns," *IEEE transactions on geoscience and remote sensing*, vol. 56, no. 5, pp. 2811–2821, 2018.
- [57] N. He, L. Fang, S. Li, J. Plaza, and A. Plaza, "Skip-connected covariance network for remote sensing scene classification," *IEEE transactions on neural networks and learning systems*, vol. 31, no. 5, pp. 1461–1474, 2019.
- [58] O. Manas, A. Lacoste, X. Giró-i Nieto, D. Vazquez, and P. Rodriguez, "Seasonal contrast: Unsupervised pre-training from uncured remote sensing data," in *Proceedings of the IEEE/CVF International Conference on Computer Vision*, 2021, pp. 9414–9423.
- [59] S. Wang, Y. Guan, and L. Shao, "Multi-granularity canonical appearance pooling for remote sensing scene classification," *IEEE Transactions on Image Processing*, vol. 29, pp. 5396–5407, 2020.
- [60] Q. Bi, K. Qin, H. Zhang, and G.-S. Xia, "Local semantic enhanced convnet for aerial scene recognition," *IEEE Transactions on Image Processing*, vol. 30, pp. 6498–6511, 2021.
- [61] G. Zhang, W. Xu, W. Zhao, C. Huang, E. N. Yk, Y. Chen, and J. Su, "A multiscale attention network for remote sensing scene images classification," *IEEE Journal of Selected Topics in Applied Earth Observations and Remote Sensing*, vol. 14, pp. 9530–9545, 2021.
- [62] S. Wang, Y. Ren, G. Parr, Y. Guan, and L. Shao, "Invariant deep compressible covariance pooling for aerial scene categorization," *IEEE Transactions on Geoscience and Remote Sensing*, vol. 59, no. 8, pp. 6549–6561, 2020.
- [63] S.-B. Chen, Q.-S. Wei, W.-Z. Wang, J. Tang, B. Luo, and Z.-Y. Wang, "Remote sensing scene classification via multi-branch local attention network," *IEEE Transactions on Image Processing*, vol. 31, pp. 99–109, 2021.
- [64] B. Li, Y. Guo, J. Yang, L. Wang, Y. Wang, and W. An, "Gated recurrent multiattention network for vhr remote sensing image classification," *IEEE Transactions on Geoscience and Remote Sensing*, vol. 60, pp. 1–13, 2021.
- [65] Y. Zhao, J. Liu, J. Yang, and Z. Wu, "Emscnet: Efficient multisample contrastive network for remote sensing image scene classification," *IEEE Transactions on Geoscience and Remote Sensing*, vol. 61, pp. 1–14, 2023.
- [66] D. Wang, Q. Zhang, Y. Xu, J. Zhang, B. Du, D. Tao, and L. Zhang, "Advancing plain vision transformer toward remote sensing foundation model," *IEEE Transactions on Geoscience and Remote Sensing*, vol. 61, pp. 1–15, 2022.
- [67] T. Nampally, J. Wu, and S. Dev, "Performance comparison of multispectral channels for land use classification," in *IGARSS 2023-2023 IEEE International Geoscience and Remote Sensing Symposium*. IEEE, 2023, pp. 6178–6181.
- [68] K. Zhang and H. Yang, "Semi-supervised multi-spectral land cover classification with multi-attention and adaptive kernel," in *2020 IEEE International Conference on Image Processing (ICIP)*. IEEE, 2020, pp. 1881–1885.
- [69] P. Gómez and G. Meoni, "Msmatch: semisupervised multispectral scene classification with few labels," *IEEE Journal of Selected Topics in Applied Earth Observations and Remote Sensing*, vol. 14, pp. 11 643–11 654, 2021.
- [70] P. Goyal, Q. Duval, I. Seessel, M. Caron, I. Misra, L. Sagun, A. Joulin, and P. Bojanowski, "Vision models are more robust and fair when pretrained on uncured images without supervision," *arXiv preprint arXiv:2202.08360*, 2022.
- [71] X. Wanyan, S. Seneviratne, S. Shen, and M. Kirley, "Dino-mc: Self-supervised contrastive learning for remote sensing imagery with multi-sized local crops," *arXiv preprint arXiv:2303.06670*, 2023.
- [72] D. Uchaev and D. Uchaev, "Small sample hyperspectral image classification based on the random patches network and recursive filtering," *Sensors*, vol. 23, no. 5, p. 2499, 2023.
- [73] H. Xie, L. Zhang, and C. P. Lim, "Evolving cnn-lstm models for time series prediction using enhanced grey wolf optimizer," *IEEE access*, vol. 8, pp. 161 519–161 541, 2020.
- [74] X. Cheng, W. Zhang, A. Wenzel, and J. Chen, "Stacked resnet-lstm and coral model for multi-site air quality prediction," *Neural Computing and Applications*, vol. 34, no. 16, pp. 13 849–13 866, 2022.
- [75] D. Li, J. Liu, and Y. Zhao, "Prediction of multi-site pm2. 5 concentrations in beijing using cnn-bi lstm with cbam," *Atmosphere*, vol. 13, no. 10, p. 1719, 2022.
- [76] D. Guo, S. Ren, S. Lu, Z. Feng, D. Tang, S. Liu, L. Zhou, N. Duan, A. Svyatkovskiy, S. Fu *et al.*, "Graphcodebert: Pre-training code representations with data flow," *arXiv preprint arXiv:2009.08366*, 2020.
- [77] R. Klokov and V. Lempitsky, "Escape from cells: Deep kd-networks for the recognition of 3d point cloud models," in *Proceedings of the IEEE international conference on computer vision*, 2017, pp. 863–872.
- [78] H. Lei, N. Akhtar, and A. Mian, "Spherical kernel for efficient graph convolution on 3d point clouds," *IEEE transactions on pattern analysis and machine intelligence*, vol. 43, no. 10, pp. 3664–3680, 2020.
- [79] C. R. Qi, L. Yi, H. Su, and L. J. Guibas, "Pointnet++: Deep hierarchical feature learning on point sets in a metric space," *Advances in neural information processing systems*, vol. 30, 2017.
- [80] J. Li, B. M. Chen, and G. H. Lee, "So-net: Self-organizing network for point cloud analysis," in *Proceedings of the IEEE conference on computer vision and pattern recognition*, 2018, pp. 9397–9406.
- [81] R. Li, Y. Zhang, D. Niu, G. Yang, N. Zafar, C. Zhang, and X. Zhao, "Pointvgg: Graph convolutional network with progressive aggregating features on point clouds," *Neurocomputing*, vol. 429, pp. 187–198, 2021.
- [82] G. Chen, M. Wang, Y. Yang, K. Yu, L. Yuan, and Y. Yue, "Pointgpt: Auto-regressively generative pre-training from point clouds," *arXiv preprint arXiv:2305.11487*, 2023.
- [83] U. Srinivas, V. Monga, and R. G. Raj, "Sar automatic target recognition using discriminative graphical models," *IEEE transactions on aerospace and electronic systems*, vol. 50, no. 1, pp. 591–606, 2014.
- [84] G. Dong, N. Wang, and G. Kuang, "Sparse representation of monogenic signal: With application to target recognition in sar images," *IEEE signal processing letters*, vol. 21, no. 8, pp. 952–956, 2014.
- [85] G. Dong and G. Kuang, "Classification on the monogenic scale space: Application to target recognition in sar image," *IEEE Transactions on Image Processing*, vol. 24, no. 8, pp. 2527–2539, 2015.
- [86] J. A. O'Sullivan, M. D. DeVore, V. Kedia, and M. I. Miller, "Sar atr performance using a conditionally gaussian model," *IEEE Transactions on Aerospace and Electronic Systems*, vol. 37, no. 1, pp. 91–108, 2001.
- [87] J.-I. Park and K.-T. Kim, "Modified polar mapping classifier for sar automatic target recognition," *IEEE Transactions on Aerospace and Electronic Systems*, vol. 50, no. 2, pp. 1092–1107, 2014.
- [88] M. Ye, X. Lan, J. Li, and P. Yuen, "Hierarchical discriminative learning for visible thermal person re-identification," in *Proceedings of the AAAI conference on artificial intelligence*, vol. 32, no. 1, 2018.

- [89] Y. Hao, N. Wang, J. Li, and X. Gao, "Hsme: Hypersphere manifold embedding for visible thermal person re-identification," in *Proceedings of the AAAI conference on artificial intelligence*, vol. 33, no. 01, 2019, pp. 8385–8392.
- [90] M. Ye, X. Lan, Z. Wang, and P. C. Yuen, "Bi-directional center-constrained top-ranking for visible thermal person re-identification," *IEEE Transactions on Information Forensics and Security*, vol. 15, pp. 407–419, 2019.
- [91] Y. Liu, M. Ott, N. Goyal, J. Du, M. Joshi, D. Chen, O. Levy, M. Lewis, L. Zettlemoyer, and V. Stoyanov, "Roberta: A robustly optimized bert pretraining approach," *arXiv preprint arXiv:1907.11692*, 2019.
- [92] J. Howard and S. Ruder, "Universal language model fine-tuning for text classification," *arXiv preprint arXiv:1801.06146*, 2018.
- [93] Q. Xie, Z. Dai, E. Hovy, T. Luong, and Q. Le, "Unsupervised data augmentation for consistency training," *Advances in neural information processing systems*, vol. 33, pp. 6256–6268, 2020.
- [94] D. S. Sachan, M. Zaheer, and R. Salakhutdinov, "Revisiting lstm networks for semi-supervised text classification via mixed objective function," in *Proceedings of the AAAI Conference on Artificial Intelligence*, vol. 33, no. 01, 2019, pp. 6940–6948.
- [95] T. Miyato, A. M. Dai, and I. Goodfellow, "Adversarial training methods for semi-supervised text classification," *arXiv preprint arXiv:1605.07725*, 2016.
- [96] I. Beltagy, M. E. Peters, and A. Cohan, "Longformer: The long-document transformer," *arXiv preprint arXiv:2004.05150*, 2020.
- [97] Z. Yang, Z. Dai, Y. Yang, J. Carbonell, R. R. Salakhutdinov, and Q. V. Le, "Xlnet: Generalized autoregressive pretraining for language understanding," *Advances in neural information processing systems*, vol. 32, 2019.
- [98] S. Ding, J. Shang, S. Wang, Y. Sun, H. Tian, H. Wu, and H. Wang, "Ernie-doc: A retrospective long-document modeling transformer," *arXiv preprint arXiv:2012.15688*, 2020.